Available online at www.sciencedirect.com

SciVerse ScienceDirect

Ceramics International 39 (2013) 7967–7973

CERAMICS INTERNATIONAL

www.elsevier.com/locate/ceramint

Co-precipitation synthesis and AC conductivity behavior of gadolinium-doped ceria

T.H. Hsieh[a], D.T. Ray[a], Y.P. Fu[b,*]

[a]Department of Resources Engineering, National Cheng Kung University, Tainan 70101, Taiwan
[b]Department of Material Science and Engineering, National Dong-Hwa University, Shou-Feng, Hualien 97401, Taiwan

Received 26 August 2011; received in revised form 17 March 2013; accepted 18 March 2013
Available online 22 March 2013

Abstract

$Ce_{0.8}Gd_{0.2}O_{1.9}$ (GDC) powder was successfully synthesized using the co-precipitation process and the powder could be sintered to more than 95% of the theoretical density. This material was characterized using impedance spectroscopy, to distinguish the behavior of the grain interior and the grain boundary. AC impedance spectroscopy analysis was performed in the temperature range 300–800 °C. An Arrhenius plot of ln ($\sigma_t T$) vs. $1/T$, for GDC sintered at 1500 °C, changes slope at around 573 °C. At low temperatures (300–573 °C), the total conductivity (σ_t) is dominated by the conductivity of the grain interior (σ_{gi}). However, at high temperatures (573–800 °C), the total conductivity (σ_t) is dominated by the conductivity of the grain boundary (σ_{gb}). The association enthalpy of the $[Gd_{Ce}^{'}-V_O^{\cdot\cdot}]$ clusters, ΔH_a, calculated from $\Delta H_a = E_{gi}^{low} - E_{gi}^{high}$, resulted equal to 0.448 eV. Elemental analysis, using inductively coupled plasma (ICP), shows that silicon exists in GDC ceramic. This suggests that the grain boundary resistance is related to the siliceous phases. These impurity SiO_2 phases mainly originates from the raw materials.
© 2013 Elsevier Ltd and Techna Group S.r.l. All rights reserved.

Keywords: A. Powders: chemical preparation; C. Ionic conductivity; D. CeO_2; E. Fuel cells

1. Introduction

Solid oxide fuel cells (SOFCs) are the subject of widespread attention, because of their high-energy conversion efficiency and low potential for pollution. High oxide-ionic-conducting solid electrolytes based on zirconia have been intensively studied [1]. In order to reduce the operational temperature from 1000 to 800 °C, or even lower, doped ceria has been considered as a solid electrolyte for moderate temperature solid oxide fuel cells [2]. $CeO_{2-\delta}$ has a fluorite structure with oxygen vacancies ($V_O^{\cdot\cdot}$) as the predominant ionic defects. The concentration of oxygen vacancies and the concomitant oxide ion conductivity of CeO_2 can be increased by the substitution of a metal with a lower valency, such as Y [3], Sm [4,5], Gd [6,7], or Ca [8]. Pure CeO_2 stoichiometric ceramics are poor oxide ion conductors. However, the ion conductivity can be improved by increasing the number of oxygen vacancies, through the substitution of gadolinium, which has a valence of less than 4+ following its substitution for Ce^{4+} the charge is compensated by oxygen vacancies. In summary, the conductivity of doped ceria is determined by its composition, its synthesis route and the sintering process [9–14].

The ionic conductivity of ceria-based electrolytes doped with various cations has been extensively studied. Yahiro et al. [15] reported that conductivity values depend on the nature of the doping element. However, the conductivity values of the doped CeO_2 used in this work was in general widely distributed. In order to interpret the experimental results, the grain boundaries were assumed to be the dominant factor in the electrical conductivity. Wang and Nowick [16] proposed that the total conductivity comprised separate contributions from the grain boundaries and the grain interior; the resistance of grain boundaries is greater than that of the grain interior, especially at low temperatures. This is due to the fact that the amorphous insulating phases appear in these grain boundaries. Faber et al. [17] reported that the activation energy of doped CeO_2 reaches a minimum, which is a function of the doping fraction in the range of 15–20 mol% and of the type of dopants used. This phenomenon may be associated with a progressive ordering of defects, as the doping fraction increases. Huang et al. [18] proposed that mobile oxygen vacancies might

*Corresponding author. Tel.: +886 3 863 4209; fax: +886 3 863 4200.
E-mail address: d887503@alumni.nthu.edu.tw (Y.P. Fu).

0272-8842/$ - see front matter © 2013 Elsevier Ltd and Techna Group S.r.l. All rights reserved.
http://dx.doi.org/10.1016/j.ceramint.2013.03.061

condense into ordered clusters in $Ce_{0.9}Gd_{0.1}O_{1.95}$, below a certain temperature range ($T=583\pm45$ °C). The results of previous research show that the conductivity of the grain boundary has an influence on the space-charge layer [19–21] and the resistive siliceous film [22–24]. An unusual result of this study is the observation of a change in the value of the activation energy, at around 573 °C. The increase in activation energy at lower temperatures is ascribed to an additional enthalpy term, due to the association between oxygen vacancies and gadolinium cations. The presence of silicon in GDC ceramic was determined using inductively coupled plasma (ICP), which suggests that resistance of the grain boundary is related to the siliceous phases. This study reports the electrical behavior of the grain interior and grain boundary, as characterized by impedance spectroscopy, and investigates the influence of gadolinium-doped CeO_2 on the performance of the grain boundary.

2. Experimental results

$Ce_{0.8}Gd_{0.2}O_{1.9}$ (GDC) powder was synthesized by using a co-precipitation method. The detailed procedure is described as follows: stoichiometric amounts of cerium nitrate hexahydrate ($Ce(NO_3)_3\cdot6H_2O$) and gadolinium nitrate hexahydrate ($Gd(NO_3)_3\cdot6H_2O$) were dissolved in distilled water and then ammonia (NH_4OH) solution was added to the solution of nitrates. Precipitates were obtained, until pH=9.5 for the mixed solution. The final concentration of the stock solution was 0.2 M, for Ce^{3+}. The resulting precipitate was vacuum-filtered and washed three times with water and ethanol. The precipitate was then dried in an oven, at 80 °C. The co-precipitated hydrate powder decomposed to a polycrystalline oxide, upon heating to 600 °C for 2 h. The oxidation of Ce^{3+} to Ce^{4+} occurred during this stage. The GDC powder was pelletized and sintered at 1500 °C for 5 h, at a programmed heating rate of 5 °C/min, and cooled to room tenperature at 3 °C/min. All of the sintered samples achieved 95% of theoretical density.

Differential scanning calorimetry (DSC; TG-DTA/DSC Setaram, Caluire, France) was used to study the crystallization characterization of co-precipitated GDC powder. The DSC measurements used heat rating, in air, of 10 °C/min, to 600 °C. A computer-interfaced X-ray powder diffractometer (XRD) with Cu K_α radiation (λ=1.5418 Å) (Rigaku Multiflex, Tokyo, Japan) was used to identify the crystalline phases. The infrared spectra of $Ce_{0.8}Gd_{0.2}O_{1.9}$ powder were recorded in the 400–4000 cm^{-1} range using KBr (Merck for spectroscopy) pellets (5 wt% sample).

The morphological features of the GDC power and the sample sintered at 1500 °C were observed using a scanning electron microscope (SEM; Hitachi S-3500H, Tokyo, Japan). Special precautions were taken, as some contaminants from the raw materials can contaminate the sintered specimen. The chemical components of a sintered specimen of $Ce_{0.8}Gd_{0.2}O_{1.9}$ were analyzed using inductively coupled plasma mass spectroscopy (ICP-MS); the concentrations of the background acceptors, aluminum, and silicon thus measured are listed in Table 1.

Table 1
Background acceptor, aluminum, and silicon in GDC measure by ICP-MS.

Element	Level (wt%)
Yttrium	0.0008
Magnesium	0.0007
Calcium	0.0015
Lanthanum	<0.005
Gadolinium	<0.005
Aluminum	0.0012
Silicon	0.0035

AC impedance measurements were conducted using an impedance analyzer SI 1260 (Solartron analytical, Hampshire, UK) in the frequency range, from 1 Hz to 10 MHz, on isothermal plateaus that were half an hour long. The measurement temperature ranged from 300 to 800 °C, with an increment of 50 °C, for which the excitation voltage was maintained at 100 mV. Silver paste was painted onto both sides of the pellet, as an electrode. The sample with silver wires attached to the electrodes was fired at 850 °C, before the measurement. to ensure good bonding between the Ag wires and the GDC pellet. The pellets were polished with 1200 grit polishing paper and cleaned with ethanol and an ultrasonic bath for 5 min, in order to remove any grease and polishing particles, before application of the paste. The AC impedance curves were fitted by Zview software, using equivalent circuits. The Arrhenius plots (plots of $\ln(\sigma T)$ vs. $10^3/T$) were constructed and the activation energies for conduction were computed. The activation energy for conduction is obtained using an Arrhenius plot of the ionic conductivity data for thermally activated conduction and is calculated according to the following equation:

$$\sigma T=\sigma_o exp\left(-\frac{E_a}{kT}\right)$$

where E_a is the activation energy for conduction, T is the absolute temperature, k is the Boltzmann constant (0.86×10^{-4} eV K^{-1}) and σ_o is a pre-exponential factor [25].

3. Results and discussion

Fig. 1 shows the DTA/TG trace for the as-dried precursor for $Ce_{0.8}Gd_{0.2}O_{1.9}$. The first weight loss, between 50 and 100 °C, is associated with an endothermic peak in the DTA curve at ~80 °C. This is ascribed to the loss of molecular water, which is absorbed on the $Ce_{0.8}Gd_{0.2}O_{1.9}$ precursor. The second abrupt weight loss, between 250 and 400 °C, is correlated with the exothermic peak at ~270 °C and is caused mainly by the decomposition of cerium hydrate to form crystalline oxide products. Finally, the weight of the as-dried precursor appears to remain almost constant above 450 °C, which indicates that beyond this temperature a single phase of $Ce_{0.8}Gd_{0.2}O_{1.9}$ is present, without any impurities such as hydrate and nitrate materials. Fig. 2 shows the IR spectra of the as-precipitated precursor for the preparation of GDC and its decomposition products. The IR spectra show the presence of OH (3500 cm^{-1}) and CO (1720 cm^{-1}) groups in the precursor.

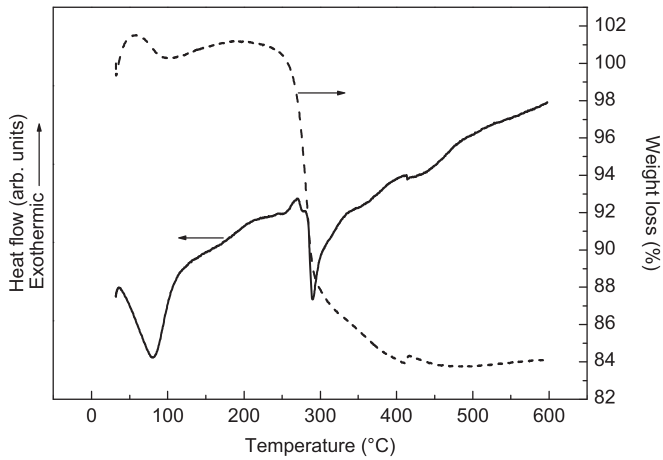

Fig. 1. DSC curves reveal the decomposition of the as-precipitated precursor for the preparation of GDC.

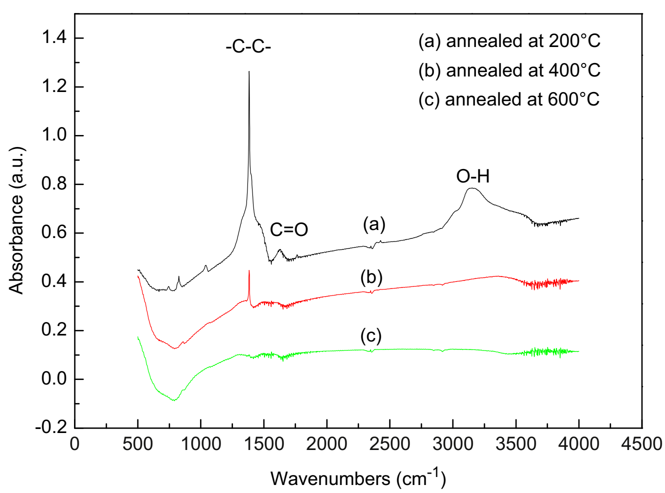

Fig. 2. IR spectra of (a) the as-precipitated precursor for the preparation of GDC, (b) the precursor annealed at 200 °C, (c) the precursor annealed at 400 °C and (d) the precursor annealed at 600 °C.

However, these functional groups are absent from the sample that was annealed at 400 and 600 °C. This indicates that the functional groups (–OH and –CO) are removed above 400 °C and the IR spectrum is similar to that of commercially available CeO_2.

High electrolytic conductivity is required, in order to avoid excessive inner resistance in a fuel cell. Ozawa [26] and Zhou and Rahaman [27] reported that nanosize CeO_2 powder shows a very different oxygen release characteristic, during sintering, compared to submicron-size powder. Therefore, this study used the co-precipitation process to produce GDC nanosize powder, in order to produce a high performance electrolyte for use in a SOFC. Fig. 3(a) shows the X-ray diffraction patterns for GDC powder, after calcinations at 600 °C, and Fig. 3(b) shows the X-ray diffraction patterns for the GDC pellet sintered at 1500 °C. The figure illustrates that the GDC powder and the sintered pellet exhibit only a cubic fluorite structure with the space group, Fm3m; no other crystalline phase is apparent. All of the peaks in the pattern match well with the Joint Committee of Powder Diffraction Standard (JCPDS) card file no. 34-0394. The crystallite size (D_{XRD}) of the GDC powder was calculated using the

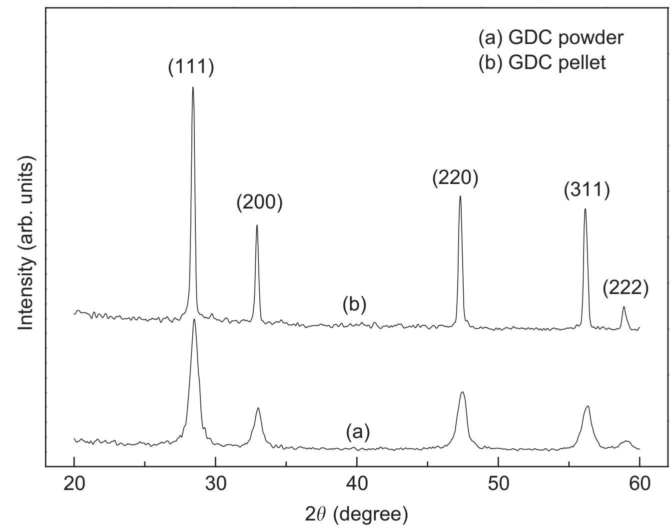

Fig. 3. XRD patterns for (a) GDC powder annealed at 600 °C and (b) GDC pellet sintered at 1500 °C.

Scherer equation, which shows that the crystallite size of GDC powder is 31.2 nm. Fig. 4 shows the microstructures of the fracture cross-section and the thermally etched pellet of GDC. As shown in Fig. 4(a) the cross-sectional image of GDC reveals a uniform grain size of about 4 μm and that the grains are connected to each other with a relative density above 95%. Fig. 4(b) shows good densification, no intra-granular pores, a well sintered pellet with a grain size ranging from 2 to 5 μm and a very uniform distribution of grain size.

Fig. 5 shows the impedance diagram for the sintered GDC pellet at 350, 500 and 650 °C. The AC impedance, measured using a two-probe method, has a contribution from the grain interior, the grain boundaries and from the electrode–electrolyte interfaces, at high, medium and low frequencies. These can be represented in the complex plane by three arcs [28]. Because of the character of the specimen, not all of these three arcs were observed at all temperatures. The values for resistance (grain interior, grain boundary and total) decreased as temperature increases. GDC with larger, semicircular grain boundaries (GB) probably results from the formation of SiO_2 impurities on the GB. The behavior at the GB may be dominated by an extrinsic effect, i.e. thin siliceous films at the grain boundary. According to the literature [28], it is possible to choose well-adapted equivalent electrical circuits to fit the impedance spectra of the electrolyte. The incomplete or small arc in the high frequency range can be attributed to grain polarization. The broad arc in the middle frequency range is due to grain boundary polarization. The spike at low frequency is ascribed to electrode polarization [29,30]. When the temperature increases, the frequency range shifts to a higher value. The grain interior, the grain boundary and the total resistances can be distinguished from the complex impedance plots.

The total resistance of the electrolyte is given by

$$R_t = R_{gi} + R_{gb}$$

where R_t is the total resistance, R_{gi} is the resistance of the grain interior and R_{gb} is the resistance of grain boundary. The simple

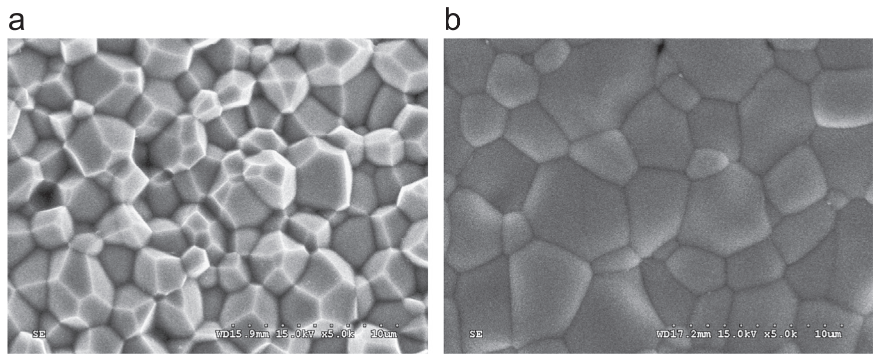

Fig. 4. SEM micrographs of GDC for (a) fracture cross-section and (b) a thermally-etched pellet sintered at 1500 °C.

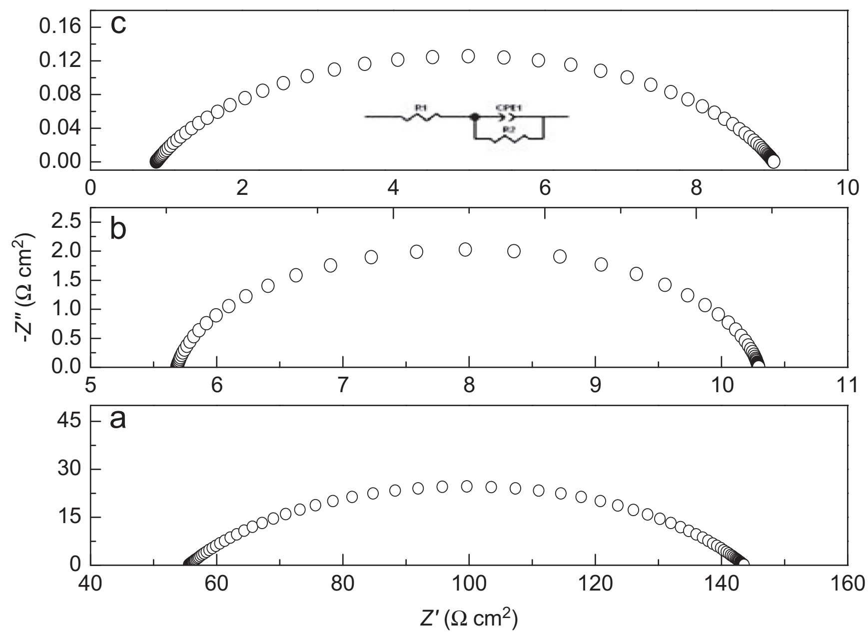

Fig. 5. AC impedance plots for the sintered GDC specimen at (a) 350 °C, (b) 500 °C and (c) 650 °C.

equivalent circuit is used for this study. A parallel RC element represents a drop capacitor with a typical relaxation time, which corresponds to the process. In this case, a constant phase element (CPE) that replaces the capacitor is used to model the experimental data. The CPE is equivalent to a distribution of capacitors in parallel. R_1 represents the resistance of the grain interior and R_2 represents the resistance of the grain boundary. The CPE can be expressed as follows: $Z = 1/C(j\omega)^n$, where C indicates the ideal capacitance (n=1), j=$(-1)^{1/2}$, ω is the angular frequency and the values of n, between 0 and 1, describe the fractal character (the heterogeneous or porous character) of the sample [28]. The relaxation frequency of the grain boundary is significantly lower at the intermediate temperature, due to a higher capacitance. Nevertheless, the conductivity of the grain interior and the grain boundary conductivities cannot be distinguished at higher temperatures. Because there is only one lower characteristic frequency term, from which only the sum of the resistance of the the grain interior and the grain boundary can be obtained, at the onset of the spike, the de-convolution of the grain interior and the contribution of the grain boundary is found at low temperature (<500 °C). These data are insufficient to analyze a typical resistance for the the grain interior and the grain boundary of GDC. In order to evaluate the bulk and grain boundary resistance at higher temperature, the grain boundary resistance (R_{gb}) is extrapolated from the total conductivity, to estimate the bulk resistance ($R_b = R_t - R_{gb}$) [31,32]. The detailed fitting parameters, R_1, R_2, CPE, and n values, as a function of temperature, are listed in Table 2. An increase in temperature causes an increase in the total conductivity. Noticeably, the conductivity of the grain boundary exhibits the same trend as that for total conductivity. The resistance of the grain boundary dominates the total resistance of the sintered GDC pellet, which indicates that the grain boundary makes the primary contribution to the total, in polycrystalline GDC. The exponents "n", which are determined from CPE models, play an important role in the interpretation of the conduction mechanism, because the n value is associated with the microstructure of the material. Grain boundaries represent a relatively homogenous resistor–capacitor system, when $n=1$. Table 2 shows that the values of the exponent, n, are distributed in the range, 0.649–0.999, as a function of temperature. When the

Table 2
Fitting parameters for impedance spectra of GDC in the temperature range 300–800 °C.

Temperature (°C)	Parameter			
	$R_1(\Omega\ cm^2)$	$R_2(\Omega\ cm^2)$	CPE (F)	n
300	113.1	290.9	3.80×10^{-5}	0.855
350	55.51	88.09	2.78×10^{-4}	0.649
400	20.55	28.72	2.86×10^{-4}	0.881
450	9.055	10.4	8.55×10^{-4}	0.886
500	5.884	4.51	2.05×10^{-3}	0.918
550	2.882	1.988	2.73×10^{-3}	0.990
600	2.147	1.039	1.60×10^{-2}	0.765
650	1.589	0.367	4.02×10^{-2}	0.764
700	1.105	0.096	4.03×10^{-2}	0.999
750	0.760	0.036	4.12×10^{-2}	0.999
800	0.561	0.010	8.09×10^{-2}	0.999

temperature is higher than 700 °C, the values of the exponent, n, are 0.999, which indicates that GDC is in a homogeneous phase at high temperatures. The capacitance of the grain boundaries is distributed as a function of temperature, from 8.09×10^{-2} to 3.80×10^{-5} F. Fig. 6 shows the conductivity of the grain interior, the grain boundary and the total conductivity, as measured from impedance spectra. The GB conductivity of Gd-doped CeO_2 ceramics is usually several orders of magnitude lower than conductivity of the grain interior (GI) [33–36], so grain boundaries block the transport of charge carriers across them. This blocking effect is solely the result of the presence of an intergranular siliceous phase. This intergranular siliceous phase was actually observed by transmission electron microscopy (TEM), as presented by Gerhardt and Nowick [37] and Tanaka et al. [38]. The ICP result, also confirms that the siliceous phase truly exists in GDC ceramics. These impure siliceous phases mainly originate from the raw materials.

For a polycrystalline oxygen-ion electrolyte, the activation energy for total ionic conduction comes from three sources, that is the enthalpy of the migration of oxygen ions (ΔH_m), the association enthalpy of complex defects (ΔH_a) and the activation energy for conduction in grain boundaries (ΔH_{gb}) [39]. These three sources simultaneously dominate the total ionic conductivity. The oxygen ionic conductivity in rare-earth-doped ceria can be represented as follows:

$$\text{At low temperature } \sigma = \frac{\sigma_0}{T} exp\left(-\frac{\Delta H_m + \Delta H_a}{kT}\right)$$

$$\text{At high temperature } \sigma = \frac{\sigma_0}{T} exp\left(-\frac{\Delta H_m}{kT}\right)$$

In the lower temperature range, charged defect associates are formed, so the activation energy for conduction, E_a, is considered to be the sum of the association enthalpy, ΔH_a, and the migration enthalpy of the oxygen ions, ΔH_m [40]. The activation energy is given as follows [31]:

$$E_{gi}^{low} = \Delta H_m + \Delta H_a$$

where ΔH_m is the enthalpy for the migration of an oxygen vacancy $[V_O^{\cdot\cdot}]$ to an equivalent near-neighbor site and ΔH_a is the association enthalpy of $[Gd_{Ce}^{'}-V_O^{\cdot\cdot}]$ clusters. However, at higher temperatures, all of the defect associates are dissociated (i.e. $\Delta H_a \to 0$) and so E_a is only dependent on ΔH_m [40]. The concentration of mobile oxygen vacancies $[V_O^{\cdot\cdot}]$ is independent of temperature; the activation energy for the motion of an oxygen vacancy in the grain interior is given as follows [31]:

$$E_{gi}^{high} = \Delta H$$

Hence, ΔH_a can be calculated from the activation energy, i.e. $\Delta H_a = E_{gi}^{low} - E_{gi}^{high}$.

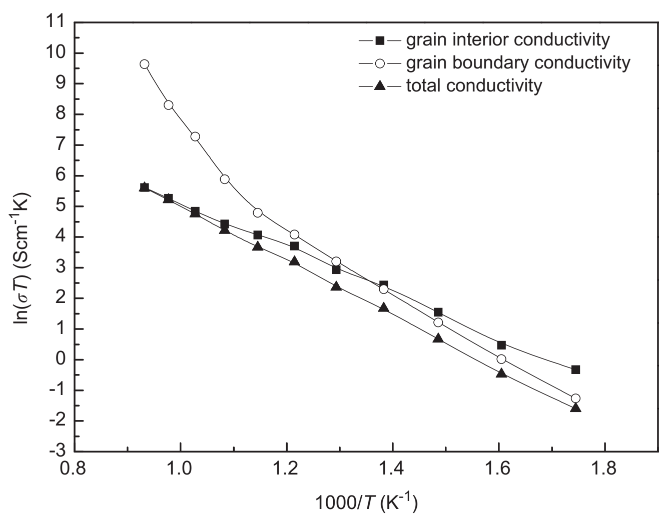

Fig. 6. Arrhenius plot of the AC impedance measurement for GDC.

The detailed conductivity of GDC for the grain interior (σ_{gi}), the grain boundary (σ_{gb}), and the total (σ_t) are summarized in Table 3. In this study, $\sigma_{gi} > \sigma_{gb}$ in the temperature range, 300–573 °C, indicating that the grain boundary conductivity (σ_{gi}) dominates the total conductivity (σ_t) at lower temperatures, but as the temperature exceeds 573 °C, $\sigma_{gb} > \sigma_{gi}$, indicating that grain interior conductivity (σ_{gb}) dominates the total conductivity (σ_t) at higher temperatures. Apparently, the GB resistance decreases as temperature increases. The contribution of GB resistance to the total resistance depends on the content of the siliceous phases, as well as on the type of

Table 3
Conductivity of GDC for the grain interior (σ_{gi}), the grain boundary (σ_{gb}) and total conductivities (σ_t) in the temperature range, 300–800 °C.

Temperature (°C)	R_{gb}/R_t	σ_t (S cm^{-1})	σ_{gi} (S cm^{-1})	σ_{gb} (S cm^{-1})
300	0.720	3.54×10^{-4}	1.26×10^{-3}	4.92×10^{-4}
350	0.613	9.96×10^{-4}	2.57×10^{-3}	1.62×10^{-3}
400	0.583	2.90×10^{-3}	6.96×10^{-3}	4.98×10^{-3}
450	0.534	7.35×10^{-3}	1.58×10^{-2}	1.37×10^{-2}
500	0.434	1.37×10^{-2}	2.43×10^{-2}	3.17×10^{-2}
550	0.408	2.93×10^{-2}	4.96×10^{-2}	7.19×10^{-2}
600	0.326	4.49×10^{-2}	6.66×10^{-2}	1.37×10^{-1}
650	0.187	7.31×10^{-2}	8.99×10^{-2}	3.89×10^{-1}
700	0.081	1.19×10^{-1}	1.29×10^{-1}	1.48
750	0.045	1.79×10^{-1}	1.88×10^{-1}	3.94
800	0.019	2.50×10^{-1}	2.55×10^{-1}	14.35

Table 4
The total activation energy (E_t), grain interior activation energy (E_{gi}) and grain boundary activation energy (E_{gb}) of GDC at low temperatures and high temperatures.

Component	Low temperatures (300–573 °C)			High temperatures (573–800 °C)		
	E_t^{low}(eV)	E_{gi}^{low}(eV)	E_{gb}^{low}(eV)	E_t^{high}(eV)	E_{gi}^{high}(eV)	E_{gb}^{high}(eV)
$Ce_{0.8}Gd_{0.2}O_{1.9}$	0.806	1.032	0.882	0.785	0.581	1.952

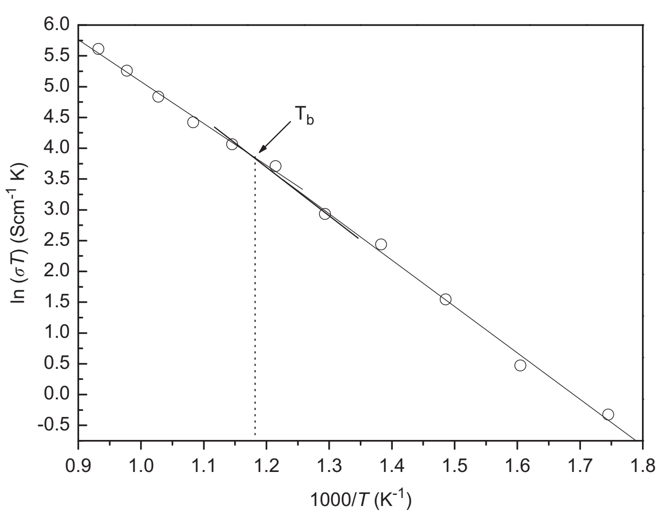

Fig. 7. Temperature dependence of the grain interior conductivity of GDC.

dopants used [32]. Table 4 shows the total activation energy (E_t), grain interior activation energy (E_{gi}) and grain boundary activation energy (E_{gb}), which indicates that the total activation energy at low temperatures (E_t^{low}), calculated from 300 to 573 °C, is almost equal to the grain boundary activation energy at low temperatures (E_{gb}^{low}). The Arrhenius plot of ln ($\sigma_t T$) vs. 1/T gives two straight lines intersecting at a critical temperature (T_b) of around 573 °C, as shown in Fig. 7. This behavior is in accordance with the result noted in reference [17]. The addition of Gd_2O_3 into the CeO_2 system leads to the formation of oxygen vacancies, because the charge compensating Gd'_{ce} may act as a nucleating center for the formation of an order-vacancy cluster, and this nucleation center has a critical temperature, T_b. The oxygen vacancies progressively form clusters, below T_b, whereas at temperatures above T_b, the vacancies are dissolved into the matrix of oxygen sites. The Arrhenius plot for the grain interior conductivity of GDC exhibits two distinct regions, each with different temperature dependence. At low temperatures (300–573 °C), the activation energy of the grain interior ($E_{gi}^{low}=1.032$ eV) is associated with the migration of extrinsic surface defects. However, at high temperatures (573–800 °C), the activation energy of the grain interior ($E_{gi}^{low}=0.581$ eV) is associated with the dissociation of defect clusters. The association enthalpy, ΔH_a, of 0.448 eV is obtained from $\Delta H_a=E_{gi}^{low}-E_{gi}^{high}$.

4. Conclusions

In this study, $Ce_{0.8}Gd_{0.2}O_{1.9}$ powder was successfully synthesized using the co-precipitation process and the powder could be sintered to achieve more than 95% of the theoretical density. Impedance spectroscopy was used to distinguish the behavior of the grain interior and the grain boundary. The Arrhenius plot of ln($\sigma_t T$) vs. 1/T gives two straight lines, which intersect at a critical temperature (T_b) of around 573 °C. As the temperature exceeds T_b, the vacancies are dissolved into the matrix of oxygen sites. As the temperature below T_b, the oxygen vacancies progressively form clusters. The association enthalpy, ΔH_a, of 0.448 eV is calculated from $\Delta H_a=E_{gi}^{low}-E_{gi}^{high}$, in which ΔH_a is the association enthalpy of $[Gd'_{Ce}-V_O^{\cdot\cdot}]$ clusters. Elemental analysis by ICP shows the existence of silicon in GDC ceramic. This suggests that the grain boundary resistance is related to the siliceous phases. These impurity SiO_2 phase originates mainly from the raw materials.

References

[1] B.C.H. Steele, Oxygen transport and exchange in oxide ceramics, Journal of Power Sources 49 (1994) 1–14.

[2] N.Q. Minh, Ceramic fuel cells, Journal of the American Ceramics Society 76 (1993) 563–588.

[3] H. Yahiro, Y. Baba, K. Eguchi, H. Arai, High-temperature fuel cell with ceria-yttria solid electrolyte, Journal of the Electrochemical Society 135 (1988) 2077–2080.

[4] T. Inoue, T. Setoguchi, K. Eguchi, H. Aria, Study of a solid-oxide fuel cell with a ceria-based solid electrolyte, Solid State Ionics 35 (1989) 285–291.

[5] C.C. Chen, M.M. Nasrallah, H.U. Anderson, Synthesis and characterization of $(CeO_2)_{0.8}$ $(SmO_{1.5})_{0.2}$ thin films for polymeric precursors, Journal of Electrochemical Society 140 (1993) 3555–3560.

[6] H. Yahiro, K. Eguchi, H. Aria, Electrical properties and reproducibilities of ceria-rare-earth oxide systems and their application to solid oxide fuel cell, Solid State Ionics 36 (1989) 71–75.

[7] D.L. Maricle, T.E. Swarr, S. Karavolis, Enhanced ceria—a low temperature SOFC electrolyte, Solid State Ionics 52 (1992) 173–182.

[8] R.N. Blumenthal, F.S. Brugner, J.E. Garnier, The electrical conductivity of CaO-doped nonstoichiometric cerium dioxide from 700 to 1500 °C, Journal of the Electrochemical Society 120 (1973) 1230–1237.

[9] K. Eguchi, T. Setoguchi, T. Inoue, H. Arai, Electrical properties of ceria based oxides and their application to solid oxide fuel-cells, Solid State Ionics 52 (1992) 165–172.

[10] H. Inaba, H. Tagawa, Review ceria-based solid electrolytes, Solid State Ionics 83 (1996) 1–16.

[11] J. Prado-Gonjal, R. Schmidt, J. Espíndola-Canuto, P. Ramos-Alvarez, E. Morán, Increased ionic conductivity in microwave hydrothermally synthesized rare-earth doped ceria $Ce_{1-x}RE_xO_{2-(x/2)}$, Journal of Power Sources 209 (2012) 163–171.

[12] M. Mogensen, N.M. Sammes, G.A. Tompsett, Physical, chemical and electrochemical properties of pure and doped ceria, Solid State Ionics 129 (2000) 63–94.

[13] Y. Zheng, S. He, L. Ge, M. Zhou, H. Chen, L. Guo, Effect of Sr on Sm-doped ceria electrolyte, International Journal of Hydrogen Energy 36 (2011) 5128–5135.

[14] J. Wright, A.V. Virkar, Conductivity of porous Sm_2O_3-doped CeO_2 as a function of temperature and oxygen partial pressure, Journal of Power Sources 196 (2011) 6118–6124.

[15] H. Yahiro, Y. Eguchi, K. Eguchi, H. Arai, Oxygen ion conductivity of the ceria-samarium oxide system with fluorite structure, Journal of Applied Electrochemistry 18 (1988) 527–531.

[16] D.Y. Wang, A.S. Nowick, The grain-boundary effect in doped ceria solid electrolytes, Journal of Solid State Chemistry 35 (1980) 325–333.

[17] J. Faber, C. Geoffroy, A. Roux, A. Sylvestre, P. Abelard, A systematic investigation of the dc electrical conductivity of rare-earth doped ceria, Applied Physics A: Materials Science and Processing 49 (1989) 225–232.

[18] K. Huang, M. Feng, J.B. Goodenough, Fabrication and characteristics of anode-supported flat-tube solid oxide fuel cell, Journal of the American Ceramics Society 81 (1998) 357–362.

[19] J. Maier, B. Bunsenges, On the conductivity of polycrystalline materials, Physical Chemistry 90 (1986) 26–33.

[20] X. Guo, Space-charge conduction in yttria and alumina codoped-zirconial, Solid State Ionics 96 (1997) 247–254.

[21] X. Guo, W. Sigle, J. Maier, Blocking grain boundaries in yttria-doped and undoped ceria ceramics of high purity, Journal of the American Ceramics Society 86 (2003) 77–87.

[22] T.S. Zhang, J. Ma, S.H. Chan, P. Hing, J.A. Kilner, Intermediate-temperature ionic conductivity of ceria-based solid solutions as a function of gadolinia and silica contents, Solid State Sciences 6 (2004) 565–572.

[23] S.P.S. Badwal, Grain boundary resistivity in zirconia-based materials: effect of sintering temperatures and impurities, Solid State Ionics 76 (1995) 67–80.

[24] M.J. Verkerk, B.J. Middelhuis, A.J. Burgraaf, Effect of grain boundaries on the conductivity of high purity ZrO_2–Y_2O_3 ceramics, Solid State Ionics 6 (1982) 159–170.

[25] C. Tian, S.W. Chan, Ionic conductivities, sintering temperatures and microstructures of bulk ceramic CeO_2 doped with Y_2O_3, Solid State Ionics 134 (2000) 89–102.

[26] M. Ozawa, Effect of oxygen release on the sintering of fine CeO_2 powder at low temperature, Scripta Materialia 50 (2004) 61–64.

[27] Y.C. Zhou, M.N. Rahaman, Effect of redox reaction on the sintering behavior of cerium oxide, Acta Materialia 45 (1997) 3635–3639.

[28] J.X. Zhu, D.F. Zhou, S.R. Guo, J.F. Ye, X.F. Hao, X.Q. Cao, J. Meng, Grain boundary conductivity of high purity neodymium-doped ceria nanosystem with and without the doping of molybdenum oxide, Journal of Power Sources 174 (2007) 114–123.

[29] J.V. Herle, D. Seneviratne, A.J. McEvoy, Lanthanide co-doping of solid electrolytes: AC conductivity behavior, Journal of the European Ceramic Society 19 (1999) 837–841.

[30] J.V. Herle, R. Vasquez, Conductivity of Mn and Ni-doped stabilized zirconia electrolyte, Journal of the European Ceramic Society 24 (2004) 1177–1180.

[31] H. Li, C. Xia, M. Zhu, Z. Zhou, G. Meng, Reactive $Ce_{0.8}Sm_{0.2}O_{1.9}$ powder synthesized by carbonate coprecipitation: sintering and electrical characteristics, Acta Materialia 54 (2006) 721–727.

[32] T.S. Zhang, J. Ma, Y.J. Leng, S.H. Chan, P. Hing, J.A. Kilner, Effect of transition metal oxides on densification and electrical properties of Si-containing $Ce_{0.8}Gd_{0.2}O_{2-\delta}$ ceramics, Solid State Ionics 168 (2004) 187–195.

[33] S.J. Hong, K. Mehta, A.V. Virkar, Effect of microstructure and composition on ionic conductivity of rare-earth oxide-doped ceria, Journal of the Electrochemical Society 145 (1998) 638–647.

[34] Y.M. Chiang, E.B. Lavik, D.A. Blom, Defect thermodynamics and electrical properties of nanocrystalline oxides: pure and doped CeO_2, Nanostructure Materials 9 (1997) 633–642.

[35] J.H. Hwang, D.S. McLachlan, T.O. Mason, Brick layer model analysis of nanoscale-to-microscale cerium dioxide, Journal of Electroceramics 3 (1999) 7–16.

[36] H.L. Tuller, Ionic conduction in nanocrystalline materials, Solid State Ionics 131 (2000) 143–157.

[37] R. Gerhardt, A.S. Nowick, Grain-boundary effect in ceria doped with trivalent cations: I Electrical measurements, Journal of the American Ceramics Society 69 (1986) 641–646.

[38] J. Tanaka, J.F. Baumard, P. Abelard, Nonlinear electrical properties of grain boundaries in an oxygen-ion conductor (CeO_2–Y_2O_3), Journal of the American Ceramics Society 70 (1987) 637–643.

[39] T.S. Zhang, J. Ma, H. Cheng, S.H. Chan, Ionic conductivity of high-purity Gd-doped ceria solid solutions, Materials Researsh Bulletin 41 (2006) 563–568.

[40] I.E.L. Stephens, J.A. Kilner, Ionic conductivity of $Ce_{1-x}Nd_xO_{2-x/2}$, Solid State Ionics 177 (2006) 669–676.